

Article

Comparative Study of the Photocatalytic Degradation of Crystal Violet Using Ferromagnetic Magnesium Oxide Nanoparticles and MgO-Bentonite Nanocomposite

Sally E. A. Elashery^{1,*}, Islam Ibrahim^{2,*}, Hassanien Gomaa³, Mohamed M. El-Bourai⁴, Ihab A. Moneam^{5,6}, Shimaa S. Fekry⁴ and Gehad G. Mohamed^{1,7}

¹ Chemistry Department, Faculty of Science, Cairo University, Giza 12613, Egypt

² Department of Chemistry, Faculty of Science, Al-Azhar University, Nasr City, Cairo 11884, Egypt

³ Department of Chemistry, Faculty of Science, Al-Azhar University, Assiut 71524, Egypt

⁴ Central Laboratory for Environmental Quality Monitoring (CLEQM), National Water Research Center (NWRC), El-Qanater El-Khairiya 13621, Egypt

⁵ Supplementary General Sciences Department, Faculty of Dentistry, Future University, New Cairo 11835, Egypt

⁶ Clinical Laboratory Sciences Department, College of Pharmacy, Al Maaqal University, Al Basrah 61015, Iraq

⁷ Nanoscience Department, Basic and Applied Sciences Institute, Egypt-Japan University of Science and Technology, New Borg El Arab, Alexandria 21932, Egypt

* Correspondence: sally_elsayed_ahmed@cu.edu.eg (S.E.A.E.); eslamebraheem_85@azhar.edu.eg (I.I.)

Abstract: In this work, the exploitation of the synthesized magnesium oxide nanoparticles and MgO-bentonite nanocomposite as an effective photocatalyst has been reported. They were utilized to study their applicability for the photocatalytic degradation of crystal violet in wastewater. Fourier-transform infrared (FTIR) spectra, X-ray powder diffraction (XRPD), energy-dispersive X-ray spectroscopy (EDX), and transmission electron microscope (TEM) were used for characterization. The photocatalytic efficiency of the synthesized photocatalysts for CV decomposition has been optimized in terms of several factors such as pH, contact time, the dose of the catalyst, and the dye concentration. The maximum degradation efficiency of CV was found to be 99.19% at the optimum state of pH value of 7, using 0.2 g of MgO NPs, while in the case of MgO-bentonite nanocomposite, the maximum degradation efficiency was decreased to 83.38%. The photocatalytic reaction mechanism was investigated using the scavenging reaction process, revealing that holes were majorly responsible for the degradation of CV. The kinetic data were suitable and best fitted by the pseudo-first-order kinetic model.

Keywords: photocatalysis; scavenger test; magnesium oxide–bentonite nanocomposite; degradation and kinetic study



Citation: Elashery, S.E.A.; Ibrahim, I.; Gomaa, H.; El-Bourai, M.M.; Moneam, I.A.; Fekry, S.S.; Mohamed, G.G. Comparative Study of the Photocatalytic Degradation of Crystal Violet Using Ferromagnetic Magnesium Oxide Nanoparticles and MgO-Bentonite Nanocomposite. *Magnetochemistry* **2023**, *9*, 56. <https://doi.org/10.3390/magnetochemistry9020056>

Academic Editors: Hamid Rashidi Nodeh, Syed Shahabuddin and Mohammad Faraji

Received: 22 January 2023

Revised: 7 February 2023

Accepted: 10 February 2023

Published: 12 February 2023



Copyright: © 2023 by the authors. Licensee MDPI, Basel, Switzerland. This article is an open access article distributed under the terms and conditions of the Creative Commons Attribution (CC BY) license (<https://creativecommons.org/licenses/by/4.0/>).

1. Introduction

Water pollution has gained a lot of attention worldwide because of the serious environmental and health impacts of wastewater from various industrial sectors [1–3]. Textile wastewater containing very low concentrations of dyes can cause waste streams to become extremely colored. These compounds are highly non-biodegradable and mutagenic, in addition to their negative visual effects [4,5]. Among these dyes, crystal violet (CV), which is included in several applications as a biological stain and veterinary drug [6], is well known for its mutagenic, teratogenic, and mitotic toxicity characteristics, as well as its low biodegradability. Moreover, because the CV is the most visible water-soluble class, the presence of CV molecules in solution, can inhibit photosynthetic activity in aquatic plants [7]. Therefore, owing to its successive usage in a wide variety of applications in addition to its negative impacts, there is an imperious necessity for CV removal. However, the removal of CV dye from wastewater can be carried out through conventional techniques such as emulsion liquid membrane separation [8], biological treatments [9], oxidation [10],

adsorption [11], and a few commonly used methods such as ultra-filtration and desalination [12]. However, these methods only succeeded in transferring organic compounds from water to another place, which needs additional management [13]. Advanced oxidation processes (AOPs) such as ozonation, photo-Fenton reactions, H_2O_2/UV , and photocatalysis processes are promising in CV decolorization [14]. Therefore, chemical treatment using AOPs [2,14–19], especially heterogeneous photocatalysis, received attention for degrading such pollutants because of the capability to totally mineralize the target pollutants [20–22].

Heterogeneous photocatalysis is a promising alternative method for eliminating organic compounds from wastewater. The wide band gap of magnesium oxide nanoparticles (MgO NPs), which enhances its catalytic activity, mechanical properties, dielectric properties, and bioactivity, has attracted a lot of attention. MgO, as a non-toxic nanoparticle, has been used in a wide variety of applications, such as its usage in crucibles or as additives in flame-retardant materials, refractory materials, and coating materials [23,24]. Because of their wide range of applications in advanced technologies, scientists have focused on synthesizing, including both nanomaterial and composite MgO [25]. Natural clay, such as bentonite, is commonly used for the removal of organic pollutants from wastewater by adsorption due to its availability and low cost [26]. Recently, in order to create distinct reaction sites and enhance the photocatalytic performance of the photocatalyst, it has been a common procedure to deposit photocatalysts on clay bentonite [27].

In the present work, the photocatalytic degradation of CV dye was investigated by using different nanoparticles and nanocomposite. The structural, morphological, spectroscopic, and photocatalytic properties of all materials and composites were thoroughly investigated. To determine the ideal circumstances for effective decomposition, we examined the impact of operational parameters on photocatalytic degradation.

2. Experimental

2.1. Materials

Magnesium chloride hexahydrate ($MgCl_2 \cdot 6H_2O$), potassium iodide, benzoquinone, isopropyl alcohol, and absolute ethanol ($\geq 99\%$) were purchased from Acros Organics. At the same time, ammonium bicarbonate (NH_4HCO_3), isopropanol, methanol, ethanol, acetone, hydrochloric acid, and sodium hydroxide were supplied by Merck. Crystal violet dye powder and bentonite were supplied by DOP ORGANIC KIMYA.

2.2. Preparation of Magnesium Oxide Nanoparticles (MgO NPs)

MgO nano-crystallites were synthesized by the hydrothermal method following the previously reported method [28,29]. Briefly, 50.83 g of $MgCl_2 \cdot 6H_2O$ was dissolved in 250 mL of distilled water and stirred for 5 min. Then, a solution of ammonium bicarbonate was prepared by dissolving 19.77 g of NH_4HCO_3 in 250 mL distilled water and then added to the first one, followed by stirring for 15 min. The obtained solution was heated at $100\text{ }^\circ\text{C}$ for 18 h, which was subsequently centrifuged for 10 min at 2500 rpm. Then, the obtained precipitate was filtered, thoroughly cleaned with distilled water and absolute ethanol, and then dried for 5 h at $70\text{ }^\circ\text{C}$ in the oven. The precipitates were then produced by calcination, which took place at $400\text{ }^\circ\text{C}$ for 3 h.

2.3. Preparation of Magnesium Oxide–Bentonite (MgO/Ben) Nanocomposite

MgO-bentonite nanocomposite has been synthesized by dispersing 1.0 g of bentonite into 100 mL distilled water under vigorous stirring for 3 h at room temperature. After that, 2.0 g of the prepared MgO NPs was dispersed in 100 mL distilled water and then added drop by drop to the bentonite solution under vigorous stirring for 12 h at room temperature. The achieved solution was subsequently heated at $200\text{ }^\circ\text{C}$ for 24 h. Then, the resulting slurry was dried at $80\text{ }^\circ\text{C}$ overnight, followed by its grinding into fine particles.

2.4. Materials Characterizations

The phase evaluation of the synthesized catalysts was performed using X-ray diffractometer (XRD, Bruker co., D8 advance, Ettlingen, Germany) and Cu radiation (1.45 Å). The XRD diffractometer was carried out at 40 mA and 40 kV with a step size of 0.02 over 2θ range of 3–70.

Energy-dispersive X-ray spectroscopy (EDX) was performed for the semi-quantitative test of the prepared catalysts using scanning electron microscope coupled with EDX unit (FESEM, Quanta FEG250, Eindhoven, The Netherlands) with acceleration voltage of 20 kV. The size of the particle and their morphology were inspected in a transmission electron microscope (TEM, HTEM, JEOL JEM 2100Plus, Tokyo, Japan), which was performed at 200 kV. The Fourier-transformed infrared (FTIR) spectra of the synthesized catalysts were obtained using NICOLET iS50 FTIR to identify the surface functional groups at ambient conditions within the wavelength range from 400 to 4000 cm⁻¹. The optical properties of the samples were analyzed by UV–Vis diffuse reflectance spectroscopy using a Hitachi 3010 spectrophotometer equipped with a 60-mm diameter integrating sphere, where BaSO₄ was used as a reference. Magnetic measurements were carried out on a Quantum Design PPMS SQUID magnetometer at 300 K.

2.5. Evaluation of the Photocatalytic Degradation Activity

Photocatalysis processes were carried out in a 500 mL borosilicate glass containing 250 mL of CV solution prepared in appropriate concentration using distilled water. To achieve an adsorption–desorption equilibrium, we stirred the solution continuously in the dark for 60 min. The irradiation was carried out using a blended metal halide lamp as a source of UV radiation, which was hung vertically on the reaction vessel in the dark box covered from the inside with aluminum foil. At specific time rates, a certain amount of the sample was withdrawn, and the prepared photocatalysts were isolated from the heterogeneous solution by centrifugation before any absorbance measurement at 3000 rpm for 10 min. The photocatalytic efficiency of CV photodegradation has been optimized in terms of several factors, such as pH, contact time, catalyst dose, and the initial dye concentration. The spectrophotometric analysis of dyes before and after the irradiation was utilized to measure the decolorization efficiency of the dye using a UV–Vis spectrophotometer at the wavelength of absorbance of CV (λ_{max} 593 nm). The degradation efficiency of the dye has been calculated as shown in Equation (1).

$$\text{Degradation \%} = [(C_0 - C_t)/C_0] \times 100 \quad (1)$$

where C₀ and C_t are the initial dye concentration and dye concentration after time t, respectively.

2.6. Scavenger Experiments

Scavenging experiments were carried out using a variety of scavengers, including KI (h⁺ quencher), IPA (OH[•] quencher), and BQ(O₂⁻ quencher), in order to explain the photocatalytic degradation mechanism of CV using UV illumination [15].

3. Results and Discussion

3.1. Structural Properties

The structural characteristics of the synthesized MgO NPs and MgO/Ben nanocomposite, in addition to pristine bentonite, have been investigated using XRD, as clarified in Figure 1a. The MgO NPs pattern reflects three peaks that were specified at (2θ) of 37.1°, 42.8°, and 62.31° that corresponded to *hkl* planes of (111), (200), and (220), respectively. All of the XRD pattern reflections can be indexed to the standard pattern of the pure cubic phase of MgO (space group: *Fm3m* (225)) (JCPDS no. 75-1525) [29]. For the bentonite clay, the characteristic peaks at diffraction angle, 2θ = 19.8°, 26.9°, 35.04° corresponds to the planes (110), (210), and (124) Miller indices [30] (JCPDS file (card no.01-088-0891)). Moreover, after the doping of MgO NPs with bentonite, new peaks were virtually specified at (2θ) of

10.76, 22.80, and 36.96 that matched to *hkl* planes of (011), (110), and (111), respectively [31], pointing to the presence of bentonite in the sample affirming the successful synthesis of MgO/Ben nanocomposite. However, the diffraction angles and relative peak intensities may have shifted due to a small compression of the bentonite crystalline structure in the presence of MgO NPs without changing the structure shape.

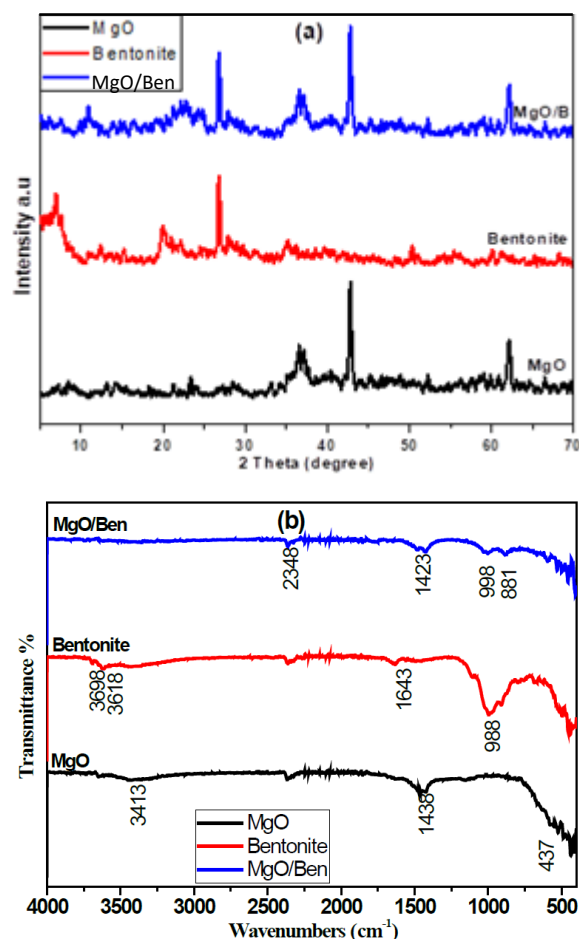


Figure 1. The XRD patterns (a), FTIR spectra (b) of the prepared MgO NPs, bentonite, and MgO/Ben nanocomposite.

In Figure 1b, FTIR spectra are shown. MgO nanoparticles exhibit two distinct absorption bands: one at 437.2 cm^{-1} , caused by MgO vibrations, and another at approximately 3413 cm^{-1} , caused by the presence of OH stretching and attributed to H_2O adsorption on the metal surface. Moreover, the absorption peak at 1438 cm^{-1} is ascribed to (C = O) stretching mode that is attributed to adsorbed (CO_2) and (CO_3^{2-}) species at the surface of MgO NPs. Consequently, these generated functional groups on the surface of MgO NPs are known to play an important role in the photocatalytic reaction process [32]. The bentonite clay spectrum revealed an absorption peak at 3618 cm^{-1} and 3698 cm^{-1} , which related to the stretching vibrations of hydroxyl groups coordinated to the octahedral cations. The Si-O stretching vibrations are responsible for the most intense absorption peak at 998 cm^{-1} [30]. Furthermore, after mixing MgO NPs with bentonite clay, the appearance of new peaks at 998.3 cm^{-1} (corresponding to stretching vibration of Si-O group), 881.9 cm^{-1} (which is related to Al-Al-OH), 530.4 and 457.4 cm^{-1} (due to Al-O-Si and Si-O-Si bending vibrations, respectively) as indicated in Figure 1b affirming the successful modification of MgO NPs with bentonite clay [33].

3.2. Electron Microscopy Characterization

The surface morphology of the prepared MgO NPs and their corresponding nanocomposite with bentonite (MgO/Ben) were examined via microscopic tools Figure 2. The TEM image of prepared MgO NPs clearly visualizes their spherical nanoscale size of an average size of 23.4 nm. However, for MgO/Ben nanocomposite, displaying the nanoscale size of the developed nanocomposite. Interestingly, the MgO NPs were decorated in a convenient dispersion regime. The elemental composition of the synthesized catalysts was further corroborated via the EDX technique in Figure 3. The elemental structure depicted in Figure 3 was verified by the EDX graph, which indicated the purity of the MgO NPs prepared using the hydrothermal method. In the case of MgO/Ben nanocomposite, the EDX graph indicated the appearance of Si and Al peaks, which are characteristic peaks for bentonite in addition to Mg and O peaks confirming the successful preparation of MgO/Ben nanocomposite.

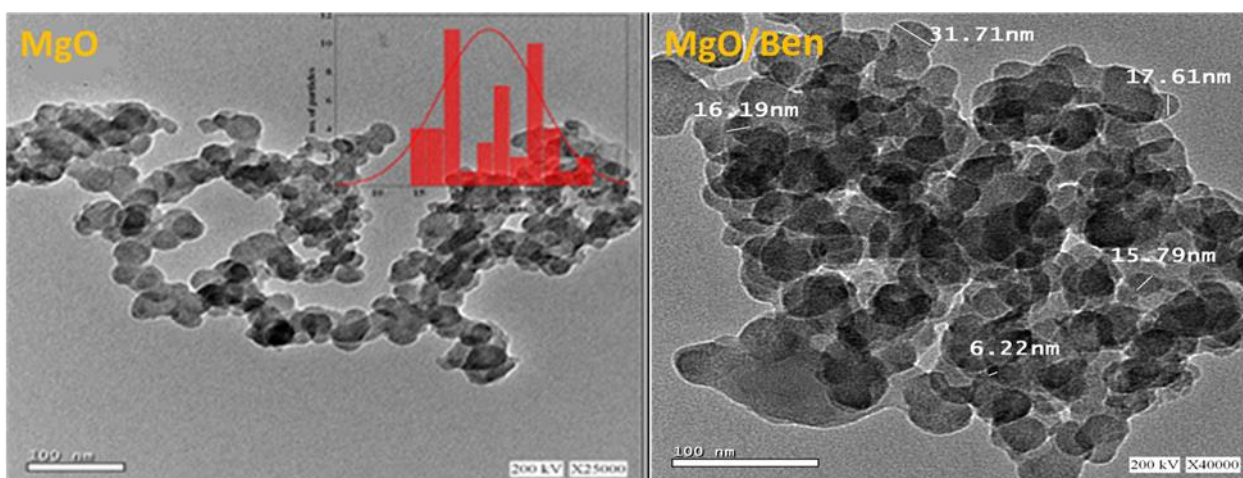


Figure 2. TEM images of MgO NPs and MgO/Ben nanocomposite.

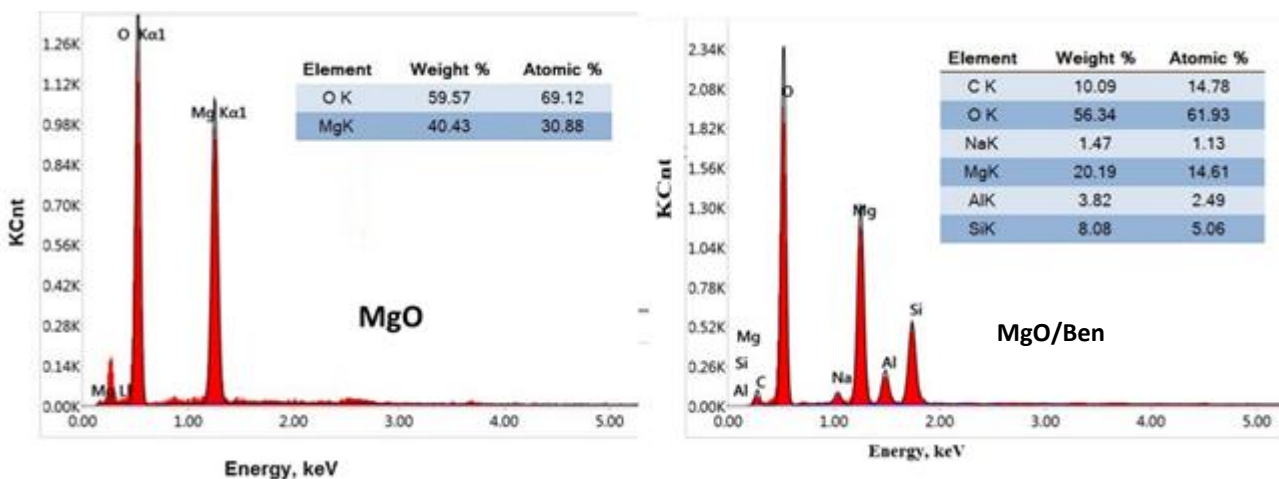


Figure 3. EDX graph of MgO NPs and MgO/Ben nanocomposite.

3.3. Magnetic Characterization

Using SQUID magnetometry, the magnetic properties of the MgO and the modified one at 300 K were studied. The MH data collected are presented in Figure 4. We discovered that MgO NPs are ferromagnetic at ambient temperature since they do not include magnetic elements like Fe and Co. The most likely cause of the current ferromagnetism is a structural fault within or on the surface of the oxide grains. Numerous additional nanoscale closed-shell oxides, including ZnO and TiO₂, have been discovered to display d0 ferromagnetism,

which is defect-related ferromagnetism. The M_s value for MgO is 8.17 emu/g, which is relatively close to the value stated in the literature [34]. In contrast, due to its dilution in the non-magnetic bentonite clay, MgO/Ben nanocomposite has lower M_s values when compared to pure MgO.

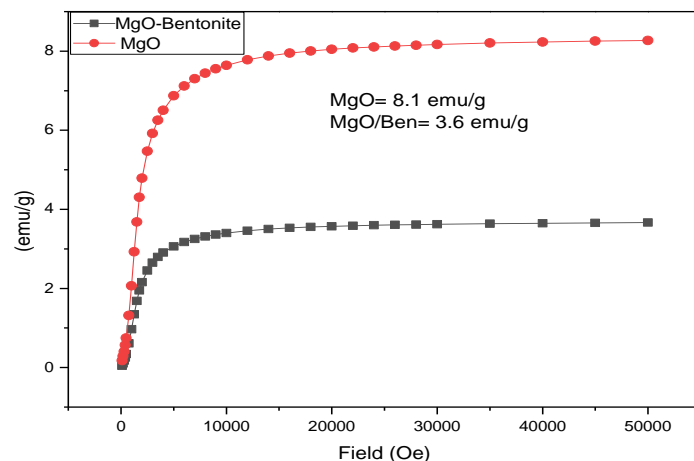


Figure 4. Magnetic properties of the prepared photocatalysts.

3.4. UV-Visible Spectroscopy

A UV-vis spectrophotometer is used to record UV-visible spectra of the prepared photocatalysts to determine the absorbance of the prepared photocatalysts. As shown in Figure 5a, the absorption peak of the prepared materials is obtained at 273 nm [35]. There is no absorbance between 400 and 800 nm, indicating that there is no absorption in the visible area. This suggests that MgO NPs and MgO/Ben nanocomposite absorb only in a narrow range of UV wavelengths.

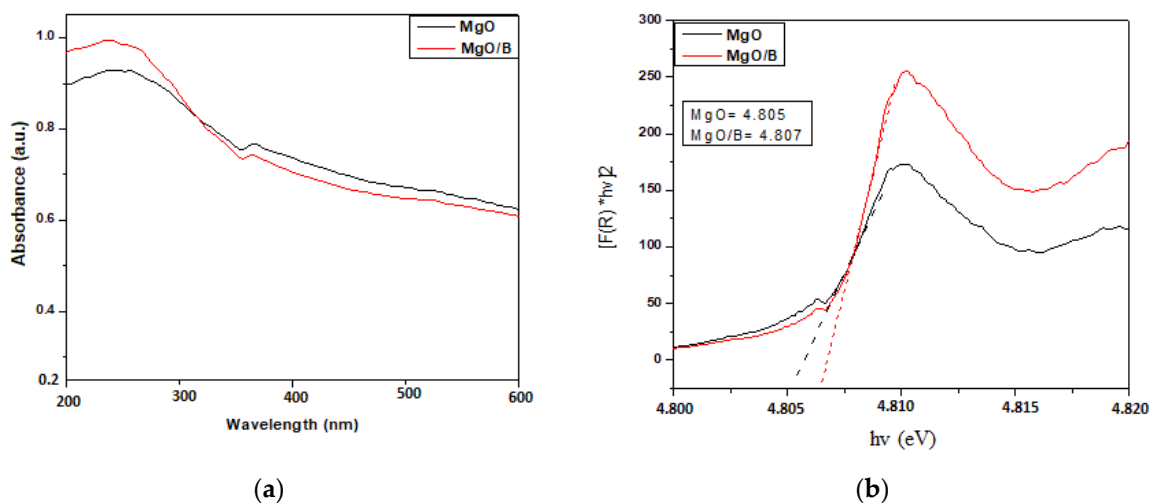


Figure 5. MgO and MgO/Ben optical absorption spectra (a); Tauc plots and estimated band gaps of the synthesized materials (b).

To calculate E_g , we analyzed the absorption spectra and calculated the absorption edge using the following approximation.

$$(\alpha hv) = A (hv - E_g)^n \quad (2)$$

where α is the absorption coefficient, h is Planck's constant, A is a constant, E_g is the energy band gap, and n is a constant that is equal to 2 for the direct band gap. Using Tauc's plot

(Figure 5b), the energy band gap is estimated, assuming a direct transition between the valence and conduction bands. The evaluated optical band gap energy of MgO NPs 4.805 eV agrees well with values from earlier reports [35], while the composite one is about 4.807 eV.

3.5. Parameters Affecting the Photocatalytic Degradation Process

3.5.1. Effect of Catalyst Dose

The photodegradation process was used to study the effect of catalyst dose (MgO NPs and MgO/Ben nanocomposite) on CV dye degradation using various doses of MgO NPs from 0.10 to 0.25 g and MgO/Ben nanocomposite from 0.10 to 0.2 g with a fixed concentration of CV solution of 10 mg L^{-1} under a stirring rate of 300 rpm after a contact time of 210 min at pH. As shown in Figure 6 and Table 1, with increasing catalyst dose, the rate of degradation increases, reaching the highest degradation efficiency of 99.19 and 83.38% using 0.2 and 0.15 g of MgO NPs and MgO/Ben nanocomposite, respectively, and then decreases. Furthermore, as the catalyst dose increases, so does agglomeration (particle–particle interaction), which is the primary cause of light absorption by the photocatalyst. Additionally, the agglomerations inhibit photons from reaching the inner surface of the catalyst. Consequently, fewer catalyst particles are excited, and thus fewer e^-/h^+ and OH \cdot radicals are produced [36].

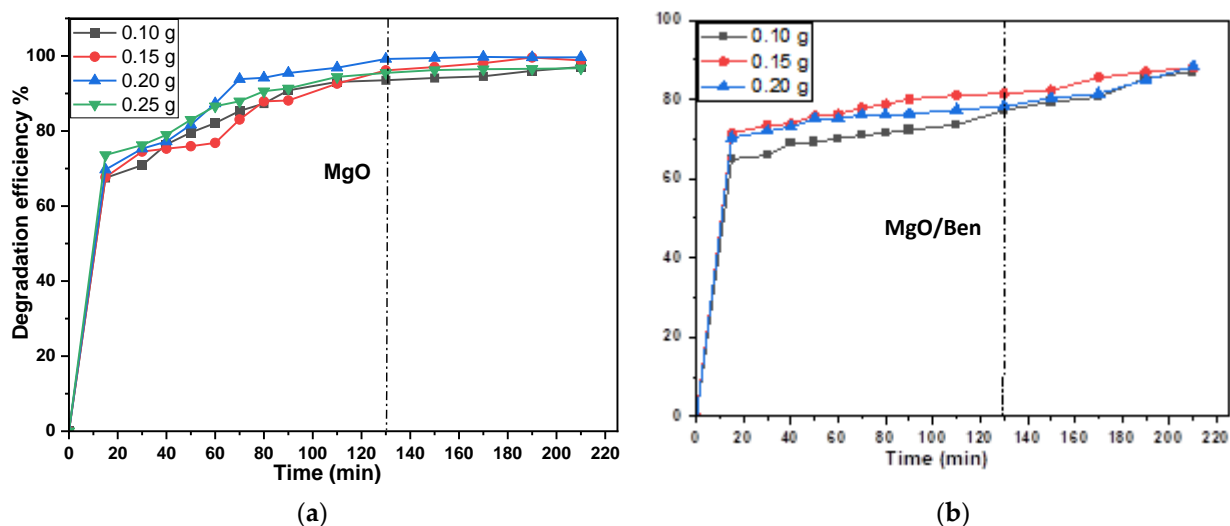


Figure 6. The catalyst dose effect on the photocatalytic degradation of CV for (a) MgO NPs and (b) MgO/Ben nanocomposite.

Table 1. Rate constants of apparent pseudo-first order, K_{ap} (min^{-1}), of degradation of CV by different catalyst doses of MgO NPs and MgO/Ben nanocomposite.

Catalyst Dose (g)	K_{ap} (min^{-1})		R^2		Degradation Efficiency %	
	MgO	MgO-Bentonite	MgO	MgO-Bentonite	MgO	MgO-Bentonite
0.10	0.0209	0.0121	0.9684	0.9661	93.52	77.25
0.15	0.0281	0.0163	0.9865	0.9866	96.14	83.38
0.20	0.0343	0.0136	0.9911	0.9794	99.19	78.19
0.25	0.0232	-	0.9847	-	95.48	-

As shown in Figure 7, the reaction kinetics of the CV were analyzed by plotting the natural log of the absorbance ratio ($\ln(A_0/A_t)$) vs. the irradiation time. Moreover, as shown in Table 1, the reaction kinetics follow apparent pseudo-first order, and the degradation rate constant was determined using the slope of the kinetic plot of CV degradation by different

doses of the synthesized photocatalysts. The solution's screening of bentonite with large particle sizes, which reduces light penetration and slows photodegradation, may be the origin of the apparent decrease in degradation rate following catalyst doping. Conversely, the lack of surface area was recognized in the case of the MgO/Ben catalyst because of agglomeration caused by particle interactions that limit the active sites [37].

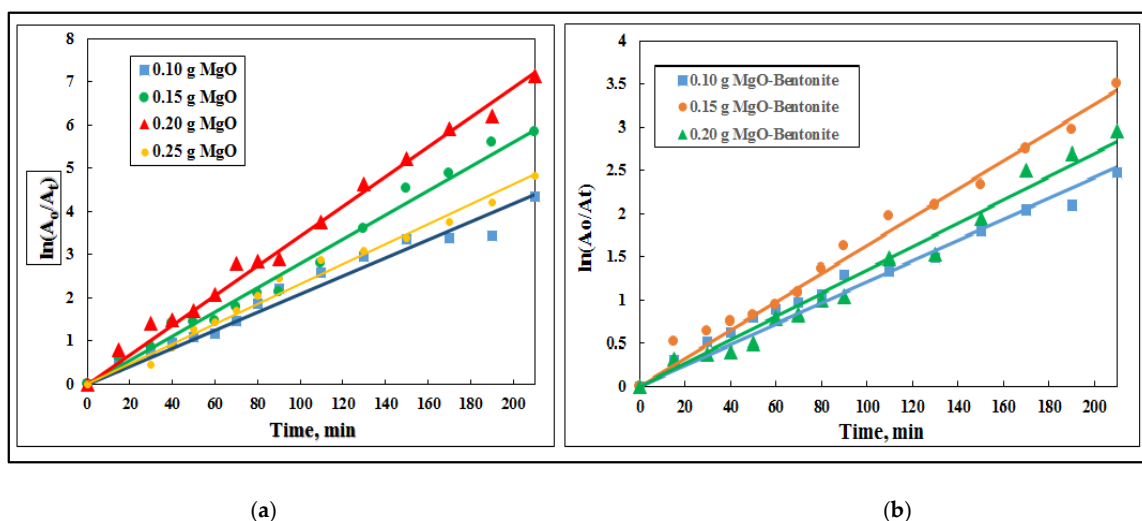


Figure 7. Plot of $\ln(A_0/A_t)$ vs. reaction time, t , at different doses of (a) MgO NPs and (b) MgO/Ben nanocomposite under the experimental conditions.

3.5.2. Contact Time Effect

The contact time effect on the photodegradation of CV was investigated at an optimum pH of 7, with a concentration of 10 mg L^{-1} and a stirring rate of 300 rpm, and with an optimum amount of MgO NPs (0.20 g) and MgO/Ben nanocomposite (0.15 g) catalysts, as shown in Figure 8 and Table 2. From the clarified data, it is clear that as contact time increases, CV degrades faster. To be more specific, the rate of photocatalytic degradation is faster for the first 130 min before equilibrium is reached. Furthermore, the presence of a significant number of active photocatalytic sites enables photocatalytic degradation to be completed in just 130 min. Following that, the repulsion between CV particles and the catalyst surface may result in a decrease in the photocatalytic degradation rate.

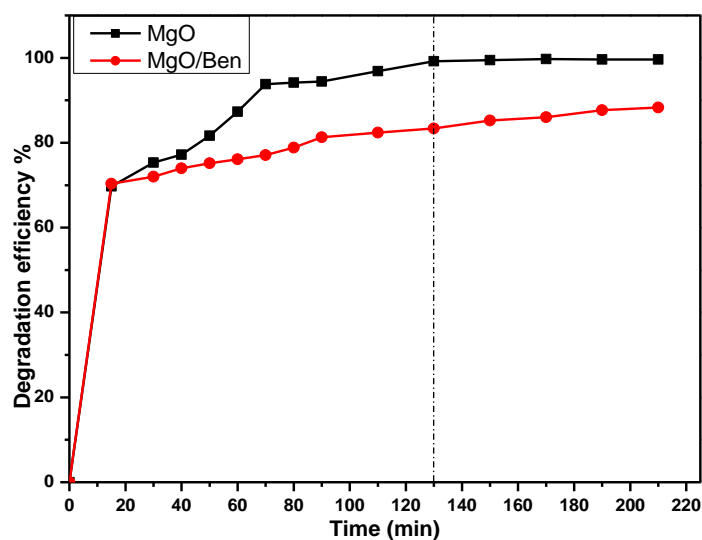


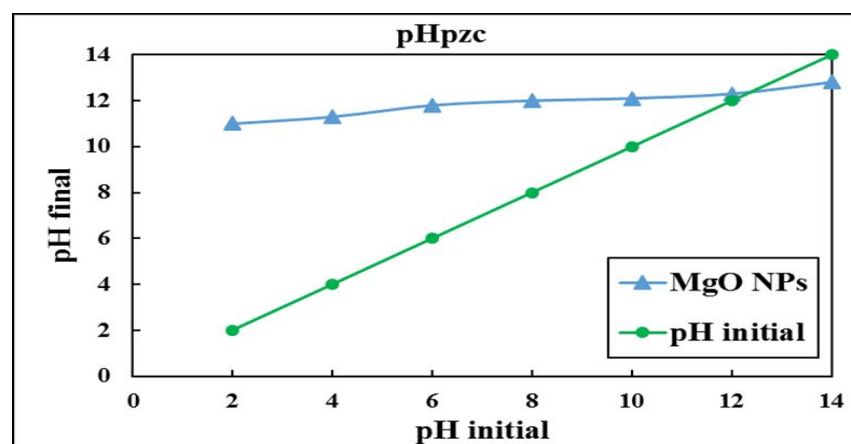
Figure 8. Contact time effect of MgO NPs (0.20 g) and MgO/Ben nanocomposite (0.15 g) on the photocatalytic degradation of CV (10 mg L^{-1}) under stirring rate of 300 rpm at pH 7.

Table 2. Effect of different contact times on the degradation efficiency of CV dye by using MgO NPs and MgO/Ben nanocomposite as a photocatalyst.

Contact Time (min)	MgO	MgO/Ben
0	0	0
15	69.69	70.34
30	75.30	71.98
40	77.18	73.99
50	81.66	75.18
60	87.31	76.09
70	93.81	77.09
80	94.10	78.83
90	94.44	81.29
110	96.86	82.39
130	99.19	83.38
150	99.46	85.21
170	99.73	86.04
190	99.59	87.68
210	99.64	88.32

3.5.3. Effect of pH

The pH is the best significant parameter for controlling the photocatalytic decomposition of CV due mainly to its effect on the catalyst surface. The pH_{pzc} of the MgO NPs catalyst was estimated at about 12.2, as shown in Figure 9. Where, at this pH, the surface has a net zero charge, while at $\text{pH} < \text{pH}_{\text{pzc}}$ and $\text{pH} > \text{pH}_{\text{pzc}}$, the surface of the catalyst is positively and negatively charged, respectively. On the other hand, the effect of pH on the photocatalytic decomposition of CV (10 mg L^{-1}) has been examined at different pH values of 3, 6, 7, and 9, as indicated in Figure 10 and Table 3 using 0.20 g of MgO NPs and 0.15 g of MgO/Ben nanocomposite as photocatalysts for a contact time of 130 min under stirring rate of 300 rpm. Where the degradation efficiency increased with the pH value increasing to pH 7, displaying the maximum efficiency of 99.19 and 83.38% for MgO NPs and MgO/Ben nanocomposite, respectively. This may be attributed to the hard deposition of CV on the catalyst surface in the acidic medium. On the other hand, in the basic medium, the CV degradation is inhibited due to the hydroxyl ion's adsorption on the catalyst surface. It is worth noting that the effect of a pH value of 11 was investigated but not taken into consideration where at such pH, the color of CV dye turned from violet to colorless without any illumination.

**Figure 9.** pH_{pzc} determination of MgO NPs.

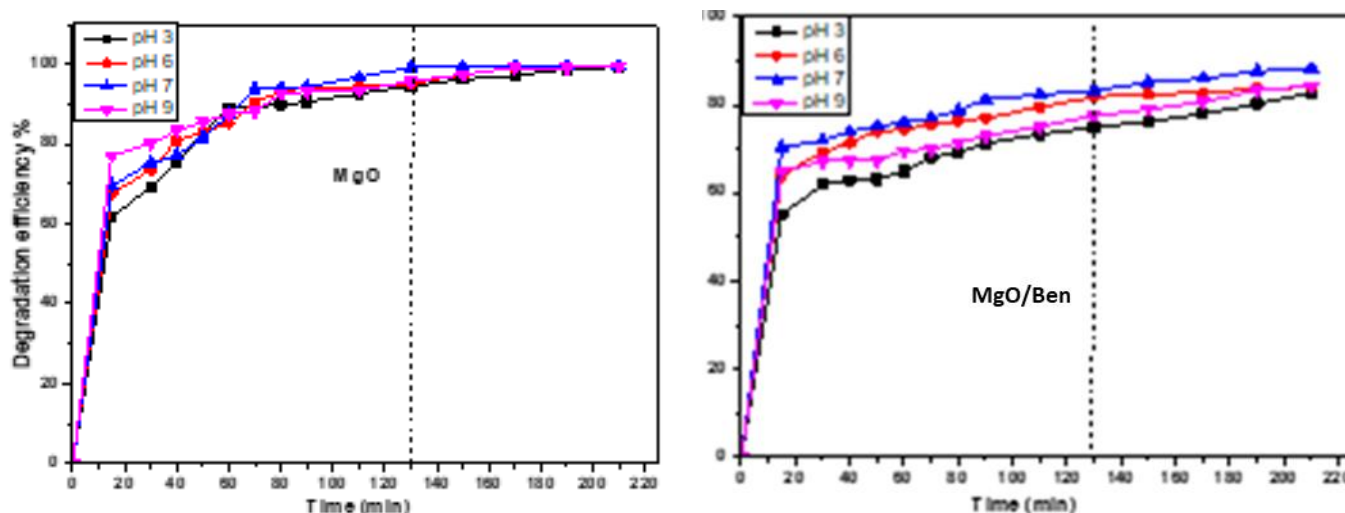


Figure 10. Effect of different pH values on the photocatalytic degradation of CV using MgO NPs and MgO/Ben nanocomposite.

Table 3. Apparent pseudo-first-order rate constants, K_{ap} (min^{-1}), of degradation of crystal violet by MgO NPs and MgO/Ben nanocomposite at different pH values.

pH	K_{ap} (min^{-1})		R^2		Degradation Efficiency %	
	MgO NPs	MgO-Bentonite Nanocomposite	MgO NPs	MgO-Bentonite Nanocomposite	MgO NPs	MgO-Bentonite Nanocomposite
3	0.0238	0.0088	0.9877	0.9876	94.58	74.87
6	0.0268	0.0113	0.9931	0.9991	95.22	81.77
7	0.0343	0.0133	0.9911	0.9885	99.19	83.38
9	0.0257	0.0105	0.9909	0.9914	95.86	77.46

The reaction kinetics of the CV was estimated by plotting the log of absorbance ratio ($\ln(A_0/A_t)$) vs. the irradiation time, as presented in Figure 11. Thus, the reaction kinetics follows pseudo-first-order kinetics, and the decomposition rate constant was calculated from the slope of the kinetic plot of degradation of CV at different pH values, as shown in Table 3.

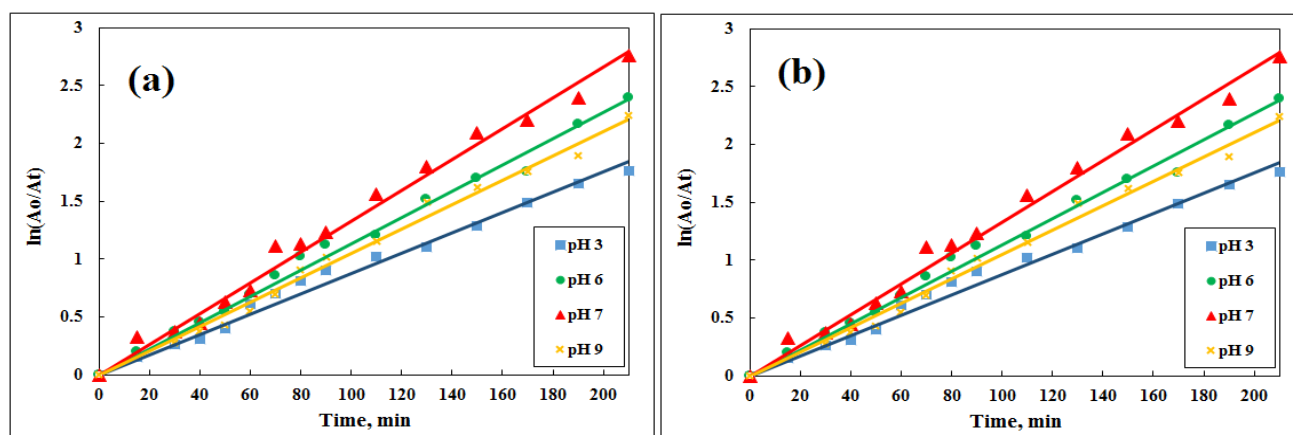


Figure 11. Plot of $\ln(A_0/A_t)$ versus reaction time, t , at different pH values under the experimental conditions using (a) 0.20 g MgO NPs and (b) 0.15 g MgO/Ben nanocomposite.

3.5.4. Effect of the Initial Dye Concentration

The initial dye concentration impact has been examined by constructing the CV photocatalytic degradation using various CV concentrations of 10, 25, and 50 mg L⁻¹ with a fixed dose of MgO NPs and MgO/Ben nanocomposite of 0.20 g and 0.15 g, respectively, at pH 7 under a stirring rate of 300 rpm for 130 min as shown in Figure 12. As indicated, the degradation efficiency of MgO NPs reached 99.19, 98.48, and 97.07% at 130 min using 10, 25, and 50 mg L⁻¹ of CV, respectively. On the other hand, MgO/Ben nanocomposite achieved a degradation efficiency of 83.38, 60.48, and 57.76% at 130 min with 10, 25, and 50 mg L⁻¹ of CV, respectively. So, the maximum degradation percentage was achieved using 10 mg L⁻¹ of CV in the case of both MgO NPs and MgO/Ben nanocomposite.

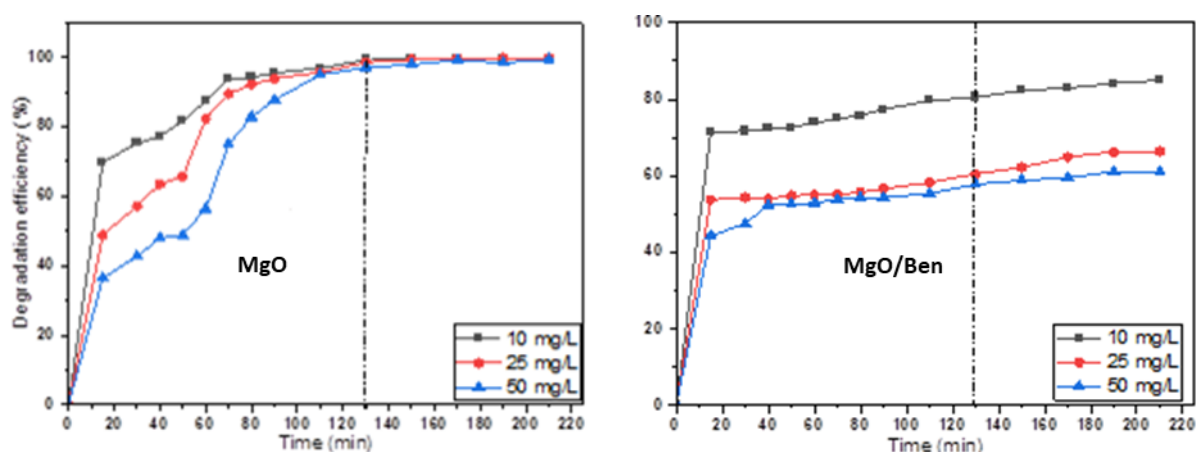


Figure 12. Effect of different initial dye concentrations on the photocatalytic degradation of CV using MgO NPs MgO/Ben nanocomposite.

Thus, as the initial dye concentration increased, the degradation efficiency slightly decreased, as presented in Table 4. This may be due to the fact that as dye concentration rises, the path length of photons entering the solution shortens, resulting in fewer photons reaching the catalyst surface and fewer catalyst molecules being excited, which causes the rate of photocatalytic degradation to increase as dye concentration falls. According to Figure 12, a significant increase in the reaction's start during the dark occurred in the case of 10 mg L⁻¹ due to adsorption–desorption, where more dye molecules adsorbed onto the photocatalyst surface, leading to a high net removal. Finally, the highest degradation efficiency achieved by MgO/Ben nanocomposite (83.38%) is still lower than that of MgO NPs (99.19%). This may be related to the bentonite deactivation or blocking of some MgO NPs active sites [38].

Table 4. The degradation efficiency of CV using MgO NPs and MgO/Ben nanocomposite at different initial dye concentrations.

Initial Dye Concentration (mg L ⁻¹)	Degradation Efficiency % (MgO NPs)	Degradation Efficiency % (MgO/Ben Nanocomposite)
10	99.19	83.38
25	98.48	60.48
50	97.07	57.76

3.5.5. Trap Experiments

The scavengers BQ (a quencher of •O₂), KI (a quencher of h⁺), and IPA (a quencher of •OH) were used to determine the reactive intermediates exposed after irradiating the MgO. As illustrated in Figure 13, the addition of KI to the CV degradation process significantly slows down the reaction process. Thus, photogenerated holes played a significant role in CV degradation, whereas the presence of IPA and BQ had no effect.

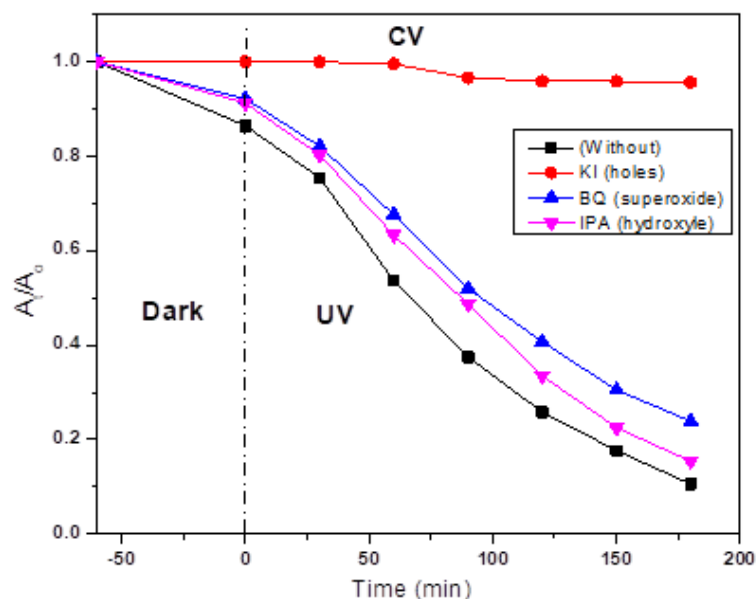


Figure 13. Scavengers affect CV photodegradation using MgO NPs under UV irradiation.

4. Comparative Study

In order to reflect the validity of the developed MgO NPs as a catalyst for CV degradation, a comparative study has been constructed between the MgO NPs and the other catalysts that have been previously reported for photocatalytic degradation of CV, as indicated in Table 5. As indicated, the cost-effective and simple catalyst of MgO NPs achieved promising degradation efficiency of 99.19%, which is superior to the other reported catalysts [39–43], using it in a lower dose of 0.20 g after a lower contact time of 2.16 h [39,41–44]. The optimum conditions for photocatalytic degradation of the dye are presented in Table 6.

Table 5. The photocatalytic degradation of crystal violet by different catalysts.

Catalyst	Degradation Efficiency %	Conditions			Ref.
		Dose (g)	Time (h)	pH	
$\text{Ga}_2\text{Zr}_{2-x}\text{W}_x\text{O}_7/\text{H}_2\text{O}_2$	100	1.00	5	9	[44]
Grafted sodium alginate/ZnO/graphene oxide	94.12	1.00	5	5	[39]
Iron–bismuth selenide–chitosan microspheres	98.95	0.20	2.5	8	[40]
Anatase Nanosphere TiO_2	99.38	—	6	7	[17]
Mn-doped and PVP-capped ZnO NPs	99.13	0.25	3	—	[41]
TG-capped ZnS NPs	87.23	0.25	3	—	[42]
Indium oxide (In_2O_3) nanocapsule	90.00	0.10	3	—	[43]
MgO NPs	99.19	0.20	2.16	7	Present work

Table 6. The optimum conditions for photocatalytic degradation of crystal violet.

Parameters	MgO NPs	MgO/Ben
pH	7	7
Initial dye concentration (mg L^{-1})	10	10
Catalyst dose (g)	0.20	0.15
Time (min)	130	130
Degradation efficiency %	99.19	83.38
Kinetics	Pseudo-first-order	Pseudo-first-order

5. Conclusions

The MgO NPs and MgO/Ben nanocomposite were synthesized, characterized, and applied for the photocatalytic degradation of CV dye as a function of pH, catalyst dose, contact time, and initial concentration of CV dye. The maximum degradation efficiency of CV (10 mg L^{-1}) was 98.19% at an optimum state of pH 7 using 0.2 g of MgO NPs after a contact time of 130 min. While the maximum degradation efficiency for 0.15 g of MgO/Ben nanocomposite was 83.38% at pH 7 using 10 mg L^{-1} of CV after 130 min of contact time. As a result, adding bentonite to MgO NPs improves CV degradation efficiency. Additionally, trapping experiments with isopropanol, benzoquinone, and KI scavengers revealed that h^+ is the major active species in the photocatalytic degradation process. Finally, MgO NPs have been synthesized using readily available and low-cost materials. As a result, this research provides a low-cost method for removing toxic dye (CV) from wastewater.

Author Contributions: Conceptualization, S.E.A.E.; methodology, S.E.A.E.; software, M.M.E.-B. and S.E.A.E.; validation, S.S.F., I.I. and G.G.M.; formal analysis, G.G.M., S.E.A.E. and M.M.E.-B.; investigation, S.E.A.E., M.M.E.-B. and I.I.; resources, S.E.A.E.; data curation, S.E.A.E., H.G. and G.G.M.; writing, S.E.A.E.; review and editing, S.S.F., I.A.M., M.M.E.-B. and G.G.M.; visualization, G.G.M. and H.G.; supervision, G.G.M.; project administration, S.E.A.E. and G.G.M. All authors have read and agreed to the published version of the manuscript.

Funding: The authors are gratefully thankful for the financial support given by Scientists for Next Generation (SNG) as a grants program from the Academy of Scientific Research and Technology (ASRT).

Institutional Review Board Statement: Not applicable.

Informed Consent Statement: Not applicable.

Data Availability Statement: Not applicable.

Acknowledgments: They would like to thank the staff of the Central Laboratory for Environmental Quality Monitoring for their cooperation.

Conflicts of Interest: The authors declare no conflict of interest.

References

1. Antoniadou, M.; Arfanis, M.; Ibrahim, I.; Falaras, P. Bifunctional $\text{g-C}_3\text{N}_4/\text{WO}_3$ Thin Films for Photocatalytic Water Purification. *Water* **2019**, *11*, 2439. [[CrossRef](#)]
2. Belessiotis, G.; Falara, P.; Ibrahim, I.; Kontos, A. Magnetic Metal Oxide-Based Photocatalysts with Integrated Silver for Water Treatment. *Materials* **2022**, *15*, 4629. [[CrossRef](#)]
3. Ibrahim, I.; Belessiotis, G.; Elseman, A.; Mohamed, M.; Ren, Y.; Salama, T.; Mohamed, M. Magnetic $\text{TiO}_2/\text{CoFe}_2\text{O}_4$ Photocatalysts for Degradation of Organic Dyes and Pharmaceuticals without Oxidants. *Nanomaterials* **2022**, *12*, 3290. [[CrossRef](#)] [[PubMed](#)]
4. Lucic, M.; Milosavljevic, N.; Radetic, M.; Saponjic, Z.; Radoicic, M.; Krusic, M.K. The potential application of TiO_2 /hydrogel nanocomposite for removal of various textile azo dyes. *Sep. Purif. Technol.* **2014**, *122*, 206–216. [[CrossRef](#)]
5. Yaseen, D.A.; Scholz, M. Textile dye wastewater characteristics and constituents of synthetic effluents: A critical review. *Int. J. Environ. Sci. Technol.* **2019**, *16*, 1193–1226. [[CrossRef](#)]
6. Guzel, F.; Saygili, H.; Saygili, G.A.; Koyuncu, F. Decolorisation of aqueous crystal violet solution by a new nanoporous carbon: Equilibrium and kinetic approach. *J. Ind. Eng. Chem.* **2014**, *20*, 3375–3386. [[CrossRef](#)]
7. Chahinez, H.O.; Abdelkader, O.; Leila, Y.; Tran, H.N. One-stage preparation of palm petiole-derived biochar: Characterization and application for adsorption of crystal violet dye in water. *Environ. Technol. Innov.* **2020**, *19*, 100872. [[CrossRef](#)]
8. Ghaemi, N.; Darabi, F.; Falsafi, M. Dye removal from water using emulsion liquid membrane: Effect of alkane solvents on efficiency. *Membr. Water Treat.* **2019**, *10*, 361–372. [[CrossRef](#)]
9. Ayed, L.; Cheriaa, J.; Laadhari, N.; Cheref, A.; Bakhrouf, A. Biodegradation of crystal violet by an isolated *Bacillus* sp. *Ann. Microbiol.* **2009**, *59*, 267–272. [[CrossRef](#)]
10. Ibrahim, I.; Ali, I.O.; Salama, T.M.; Bahgat, A.A.; Mohamed, M.M. Synthesis of magnetically recyclable spinel ferrite (MFe_2O_4 , $\text{M} = \text{Zn, Co, Mn}$) nanocrystals engineered by sol gel-hydrothermal technology: High catalytic performances for nitroarenes reduction. *Appl. Catal. B-Environ.* **2016**, *181*, 389–402. [[CrossRef](#)]
11. Foroutan, R.; Peighambaroust, S.J.; Peighambaroust, S.H.; Pateiro, M.; Lorenzo, J.M. Adsorption of Crystal Violet Dye Using Activated Carbon of Lemon Wood and Activated Carbon/ Fe_3O_4 Magnetic Nanocomposite from Aqueous Solutions: A Kinetic, Equilibrium and Thermodynamic Study. *Molecules* **2021**, *26*, 2241. [[CrossRef](#)] [[PubMed](#)]

12. Patel, A.; Soni, S.; Mittal, J.; Mittal, A.; Arora, C. Sequestration of crystal violet from aqueous solution using ash of black turmeric rhizome. *Desalination Water Treat.* **2021**, *220*, 342–352. [[CrossRef](#)]
13. Han, F.; Kambala, V.S.R.; Srinivasan, M.; Rajarathnam, D.; Naidu, R. Tailored titanium dioxide photocatalysts for the degradation of organic dyes in wastewater treatment: A review. *Appl. Catal. A-Gen.* **2009**, *359*, 25–40. [[CrossRef](#)]
14. Ibrahim, I.; Athanasekou, C.; Manolis, G.; Kaltzoglou, A.; Nasikas, N.K.; Katsaros, F.; Devlin, E.; Kontos, A.G.; Falaras, P. Photocatalysis as an advanced reduction process (ARP): The reduction of 4-nitrophenol using titania nanotubes-ferrite nanocomposites. *J. Hazard. Mater.* **2019**, *372*, 37–44. [[CrossRef](#)] [[PubMed](#)]
15. Ibrahim, I.; Kaltzoglou, A.; Athanasekou, C.; Katsaros, F.; Devlin, E.; Kontos, A.G.; Ioannidis, N.; Perraki, M.; Tsakiridis, P.; Sygellou, L.; et al. Magnetically separable TiO₂/CoFe₂O₄/Ag nanocomposites for the photocatalytic reduction of hexavalent chromium pollutant under UV and artificial solar light. *Chem. Eng. J.* **2020**, *381*, 122730. [[CrossRef](#)]
16. Mohamed, M.M.; Ibrahim, I.; Salama, T.M. Rational design of manganese ferrite-graphene hybrid photocatalysts: Efficient water splitting and effective elimination of organic pollutants. *Appl. Catal. A-Gen.* **2016**, *524*, 182–191. [[CrossRef](#)]
17. Ibrahim, I.; Belessiotis, G.V.; Antoniadou, M.; Kaltzoglou, A.; Sakellis, E.; Katsaros, F.; Sygellou, L.; Arfanis, M.K.; Salama, T.M.; Falaras, P. Silver decorated TiO₂/g-C₃N₄ bifunctional nanocomposites for photocatalytic elimination of water pollutants under UV and artificial solar light. *Results Eng.* **2022**, *14*, 100470. [[CrossRef](#)]
18. Ibrahim, I.; Belessiotis, G.V.; Arfanis, M.K.; Athanasekou, C.; Philippopoulos, A.I.; Mitsopoulou, C.A.; Romanos, G.E.; Falaras, P. Surfactant Effects on the Synthesis of Redox Bifunctional V₂O₅ Photocatalysts. *Materials* **2020**, *13*, 4665. [[CrossRef](#)]
19. Liu, C.; Mao, S.; Wang, H.L.; Wu, Y.; Wang, F.Y.; Xia, M.Z.; Chen, Q. Peroxymonosulfate-assisted for facilitating photocatalytic degradation performance of 2D/2D WO₃/BiOBr S-scheme heterojunction. *Chem. Eng. J.* **2022**, *430*, 132806. [[CrossRef](#)]
20. Ahmad, S.; Yasin, A. Photocatalytic degradation of deltamethrin by using Cu/TiO₂/bentonite composite. *Arab. J. Chem.* **2020**, *13*, 8481–8488. [[CrossRef](#)]
21. Rashad, S.; Zaki, A.H.; Farghali, A.A. Morphological effect of titanate nanostructures on the photocatalytic degradation of crystal violet. *Nanomater. Nanotechnol.* **2019**, *9*, 1847980418821778. [[CrossRef](#)]
22. El Bouraie, M.; Ibrahim, S. Differentiation Between Metronidazole Residues Disposal by Using Adsorption and Photodegradation Processes Onto MgO Nanoparticles. *Int. J. Nanomed.* **2020**, *15*, 7117–7141. [[CrossRef](#)] [[PubMed](#)]
23. Suresh, S.; Arivuoli, D. Synthesis and characterization of Pb⁺ doped MgO nanocrystalline particles. *Dig. J. Nanomater. Biostruct.* **2011**, *6*, 1597–1603.
24. Camtakan, Z.; Erenturk, S.; Yusan, S. Magnesium oxide nanoparticles: Preparation, characterization, and uranium sorption properties. *Environ. Prog. Sustain. Energy* **2012**, *31*, 536–543. [[CrossRef](#)]
25. Mohan, S.; Vellakkat, M.; Aravind, A.; Reka, U. Hydrothermal synthesis and characterization of Zinc Oxide nanoparticles of various shapes under different reaction conditions. *Nano Express* **2020**, *1*. [[CrossRef](#)]
26. Al-Shahrani, S. Phenomena of Removal of Crystal Violet from Wastewater Using Khulays Natural Bentonite. *J. Chem.* **2020**, *2020*, 4607657. [[CrossRef](#)]
27. Wang, Q.; Rhimi, B.; Wang, H.; Wang, C.Y. Efficient photocatalytic degradation of gaseous toluene over F-doped TiO₂/exfoliated bentonite. *Appl. Surf. Sci.* **2020**, *530*, 147286. [[CrossRef](#)]
28. Wang, Z.; Xu, C.L.; Wang, H.F. A Facile Preparation of Highly Active Au/MgO Catalysts for Aerobic Oxidation of Benzyl Alcohol. *Catal. Lett.* **2014**, *144*, 1919–1929. [[CrossRef](#)]
29. Raghavendra, M.; Lalithamba, H.S.; Sharath, B.S.; Rajanaika, H. Synthesis of N-alpha-protected formamides from amino acids using MgO nano catalyst: Study of molecular docking and antibacterial activity. *Sci. Iran.* **2017**, *24*, 3002–3013. [[CrossRef](#)]
30. Hebbar, R.S.; Isloor, A.M.; Prabhu, B.; Inamuddin; Asiri, A.M.; Ismail, A.F. Removal of metal ions and humic acids through polyetherimide membrane with grafted bentonite clay. *Sci. Rep.* **2018**, *8*, 4665. [[CrossRef](#)]
31. Silva, I.A.; Costa, J.M.R.; Menezes, R.R.; Ferreira, H.S.; Neves, G.D.; Ferreira, H.C. Studies of new occurrences of bentonite clays in the State of Paraiba for use in water based drilling fluids. *Rem-Rev. Escola De Minas* **2013**, *66*, 485–491. [[CrossRef](#)]
32. Taourati, R.; Khaddor, M.; Laghzal, A.; El Kasm, A. Facile one-step synthesis of highly efficient single oxide nanoparticles for photocatalytic application. *Sci. Afr.* **2020**, *8*, e00305. [[CrossRef](#)]
33. Anaissi, F.J.; Demets, G.J.F.; Toma, H.E.; Dovidauskas, S.; Coelho, A.C.V. Characterization and properties of mixed bentonite-vanadium(V) oxide xerogels. *Mater. Res. Bull.* **2001**, *36*, 289–306. [[CrossRef](#)]
34. Uchino, T. *Optical and Magnetic Properties of Defective MgO Microcrystals*; The Electrochemical Society: Pennington, NJ, USA, 2013; pp. 657–8501.
35. Mohandes, F.; Davar, F.; Salavati-Niasari, M. Magnesium oxide nanocrystals via thermal decomposition of magnesium oxalate. *J. Phys. Chem. Solids* **2010**, *71*, 1623–1628. [[CrossRef](#)]
36. Khairnar, S.D.; Patil, M.R.; Shrivastava, V.S. Hydrothermally synthesized nanocrystalline Nb₂O₅ and its visible-light photocatalytic activity for the degradation of congo red and methylene blue. *Iran. J. Catal.* **2018**, *8*, 143–150.
37. Phan, T.T.N.; Nikoloski, A.N.; Bahri, P.A.; Li, D. Heterogeneous photo-Fenton degradation of organics using highly efficient Cu-doped LaFeO₃ under visible light. *J. Ind. Eng. Chem.* **2018**, *61*, 53–64. [[CrossRef](#)]
38. Serpone, N. Heterogeneous Photocatalysis and Prospects of TiO₂-Based Photocatalytic DeNO_xing the Atmospheric Environment. *Catalysts* **2018**, *8*, 553. [[CrossRef](#)]

39. Mohamed, S.K.; Hegazy, S.H.; Abdelwahab, N.A.; Ramadan, A.M. Coupled adsorption-photocatalytic degradation of crystal violet under sunlight using chemically synthesized grafted sodium alginate/ZnO/graphene oxide composite. *Int. J. Biol. Macromol.* **2018**, *108*, 1185–1198. [[CrossRef](#)]
40. Ahmad, W.; Khan, A.; Ali, N.; Khan, S.; Uddin, S.; Malik, S.; Khan, H.; Bilal, M. Photocatalytic degradation of crystal violet dye under sunlight by chitosan-encapsulated ternary metal selenide microspheres. *Environ. Sci. Pollut. Res.* **2021**, *28*, 8074–8087. [[CrossRef](#)]
41. Mittal, M.; Sharma, M.; Pandey, O.P. Photocatalytic Studies of Crystal Violet Dye Using Mn Doped and PVP Capped ZnO Nanoparticles. *J. Nanosci. Nanotechnol.* **2014**, *14*, 2725–2733. [[CrossRef](#)]
42. Sharma, M.; Jain, T.; Singh, S.; Pandey, O.P. Photocatalytic degradation of organic dyes under UV-Visible light using capped ZnS nanoparticles. *Sol. Energy* **2012**, *86*, 626–633. [[CrossRef](#)]
43. Pawar, K.K.; Chaudhary, L.S.; Mali, S.S.; Bhat, T.S.; Sheikh, A.D.; Hong, C.K.; Patil, P.S. In₂O₃ nanocapsules for rapid photodegradation of crystal violet dye under sunlight. *J. Colloid Interface Sci.* **2020**, *561*, 287–297. [[CrossRef](#)] [[PubMed](#)]
44. Abbas, H.A.; Nasr, R.A.; Abu-Zurayk, R.; Al Bawab, A.; Jamil, T.S. Decolourization of crystal violet using nano-sized novel fluorite structure Ga₂Zr_{2-x}W_xO₇ photocatalyst under visible light irradiation. *R. Soc. Open Sci.* **2020**, *7*, 191632. [[CrossRef](#)] [[PubMed](#)]

Disclaimer/Publisher’s Note: The statements, opinions and data contained in all publications are solely those of the individual author(s) and contributor(s) and not of MDPI and/or the editor(s). MDPI and/or the editor(s) disclaim responsibility for any injury to people or property resulting from any ideas, methods, instructions or products referred to in the content.